Fluid-rich subducting topography generates anomalous forearc porosity

Christine Chesley[1], Samer Naif[2], Kerry Key[1], and Dan Bassett[3]

[1]Lamont-Doherty Earth Observatory, Columbia University, Palisades, New York, USA

[2]School of Earth and Atmospheric Sciences, Georgia Institute of Technology, Atlanta, Georgia, USA

[3]GNS Science, Lower Hutt, New Zealand

Corresponding author: Christine Chesley, chesley@ldeo.columbia.edu

The role of subducting topography on the mode of fault slip, particularly whether it hinders or facilitates large megathrust earthquakes, remains a controversial topic in subduction dynamics[1–5]. Models illustrate the potential for subducting topography to severely alter the structure, stress-state and mechanics of subduction zones[4,6], however, direct geophysical imaging of the complex fracture networks proposed and the hydrology of both the subducting topography and associated upper plate damage zones remains elusive. Here we use passive and controlled-source seafloor electromagnetic data collected at the northern Hikurangi Margin, New Zealand, to constrain electrical resistivity in a region of active seamount subduction. We show that a seamount on the incoming plate contains a thin, low porosity basaltic cap that traps a conductive matrix of porous volcaniclastics and altered material over a resistive core, which allows 3.2—4.7x more water than normal, unfaulted oceanic lithosphere to subduct. In the forearc, we image a sediment-starved plate interface above a subducting seamount with similar electrical structure to the incoming plate seamount. A sharp resistive peak within the subducting seamount lies directly beneath a prominent upper plate conductive anomaly. The coincidence of this upper plate anomaly with the location of burst-type repeating earthquakes and seismicity associated with a recent slow slip event[7], directly links subducting topography to the creation of fluid-rich damage zones in the forearc that alter the effective normal stress at the plate interface by modulating fluid overpressure. In addition to severely modifying the structure and physical conditions of the upper plate, subducting seamounts represent an underappreciated mechanism for transporting a considerable flux of water to the forearc and deeper mantle.

Observations of aseismic creep, microseismicity, and slow earthquakes at subduction zones with substantial seafloor roughness on the incoming plate[3,7] contradict the notion that subducting topography should promote strong interseismic coupling and large megathrust earthquakes[1,2]. Indeed, integrated geophysical observations reveal subducted topography in areas with weak interseismic coupling and slow slip[5,7,8]. Analogue models show that the geometric incompatibility of subducting topographic relief is accommodated by the generation of complex fracture networks in the overriding plate. These fault networks are unlikely to be conducive to earthquakes rupturing over large areas and are more likely to slip through a combination of small-earthquakes and creep[4,6]. Although the surficial scars of these damage zones have been imaged in multi-beam bathymetric data[9], the inherent structural complexity of subduction forearcs makes the extent of these fracture networks and their impact on hydrology difficult to resolve with traditional geophysical techniques. Additionally, few have speculated about how the internal composition of the subducting topography may impact subduction dynamics.

We collected magnetotelluric (MT) and controlled-source electromagnetic (CSEM) data at 29 stations along a 90-km-long trench-perpendicular profile offshore the northern Hikurangi Margin, New Zealand to study the electrical resistivity structure of the incoming plate and forearc in a region of well-documented seamount subduction[8–11] (Fig. 1). Electromagnetic data are particularly sensitive to the presence of conductive phases, especially fluids in pore spaces and fractures of otherwise low porosity material, making them a powerful tool for imaging fluid saturated sediment and damaged lithospheric rock in addition to crystalline basement[12–16]. The co-location of our EM profile with previously collected seismic reflection data[17], IODP coring sites[18] and ocean bottom seismometers[19] provides an unprecedented opportunity to test the predictions of numerical models to improve our understanding of how subducting topography influences subduction processes.

At the Hikurangi Margin, the Pacific Plate that subducts beneath the Australian Plate (Fig. 1a) is thickened relative to normal oceanic lithosphere by the Hikurangi Plateau, an Early Cretaceous Large Igneous Province thought to have been emplaced concurrently with the Ontong Java and Manihiki Plateaus[20]. The thickness of sediments that cover the plateau decreases from ~6 km in south Hikurangi to ~1 km in the north and this reduction coincides with an increased density of seamounts expressed on the seafloor to the north[10] (Fig. 1a). Along-strike variations in interseismic coupling and the depth, duration, and frequency of slow slip events (SSEs) at the margin have been identified in previous works[10], but their cause remains poorly understood.

Electrical resistivity of a seamount

We jointly modeled the 1-D and 2-D compatible MT and CSEM responses using a 2-D nonlinear, regularized inversion that solved for the vertically transverse isotropic resistivity tensor[21] (see METHODS). The resistivity structure of the incoming plate (Fig. 2a & d and Extended Data Fig. 1) is dominated by Tūranganui Knoll, one of many guyot-like features interpreted to have formed during intraplate volcanism 89—99 Ma[22]. Tūranganui Knoll is characterized by a resistive core (≥ 300 Ω-m; R1p) overlain by a more conductive matrix (C1p), which is in turn topped by a resistive cap (30—300 Ω-m; R2p) and a veneer of highly conductive marine sediments and volcaniclastics[23]. The resistivity of R2p is consistent with lower porosity extrusive basalts and dikes[13] or sills, while the existence of R1p suggests the preservation of low porosity gabbros. Coralline algae and bivalve shell fragments at IODP Site U1526 along with the steep-sided morphology of Tūranganui Knoll indicate a shallow-water history for the Knoll and its erosion to sea level[23]. We therefore posit that R2p formed subaerially from slowly cooled massive flows, making it relatively less porous and less permeable than typical extrusive basalts. C1p is a more porous amalgam likely containing volcaniclastics, pre-eruptive marine sediments, and conductive mineral assemblages from hydrothermal alteration[24].

A prominent, sub-vertical conductor (C2p) that cuts through the flank of Tūranganui Knoll corresponds to a normal fault that has been interpreted from seismic reflection data[11] (Fig. 2). This conductor is similar to anomalies seen for outer rise bending faults at the Middle America Trench[13,14], with low resistivity indicating the fault is likely a porous conduit for fluid flow. The lack of sediments above Tūranganui Knoll likely permits a more direct pathway for fluid infiltration and thus leads to higher conductivity within the fault. Heat flow data[25] show a sharp decrease below average background values over the fault and elevated values above one of Tūranganui Knoll's central cones (Fig. 2a & b), further suggesting that Tūranganui Knoll is a site of active hydrothermal recharge and discharge[25,26].

Because the resistivity of oceanic crust is primarily controlled by its porosity, we use the empirical Archie's law[27] to convert our resistivity model to porosity (Fig. 2b; Extended Data Fig. 2; and METHODS). Tūranganui Knoll feature C1p is significantly more conductive than normal oceanic crust[13,16] and correspondingly has a higher porosity than typical crust[12,13,28]. Given the spatial extent of Tūranganui Knoll (~447 km^2), our average porosity estimates for the upper 3 km of Tūranganui Knoll (9.2%—13.2%) suggest it will carry roughly 123—177 km^3 of water into the subduction zone. By comparison, an equivalent volume of normal, unfaulted oceanic crust transports only about 38 km^3 of water to the trench[13]. This calculation shows that subducting topography is an important and as yet unrecognized vessel for delivering at least 3.2—4.7x more water to the forearc and mantle wedge, where it may impact fault slip behavior and contribute to wedge serpentinization, or be carried deeper to promote hydrous melting.

Northwest of Tūranganui Knoll, the Hikurangi Trough is filled with 1.5 km of conductive sediments that correspond to siliclastic and pelagic sequences drilled at IODP Site U1520[29]. The underlying sequence of volcanics and volcaniclastics is characterised by high conductivity within 150—550 m of the base of Seismic Unit 8 (SU8; Fig. 2) and 530 m of resistive material (R2.5p), which may be a continuation of R2p from basalt flows off the flank of Tūranganui Knoll. Beneath R2.5p is a 600 m thick conductive package (C3p) that we interpret as porous sediments buried beneath the basalt flow. The deeper resistive layer corresponds to the top of the Hikurangi Plateau. Both R2.5p and C3p are truncated where volcanic cones are imaged beneath Hikurangi Trough, possibly indicating that these features have been overprinted by late-stage volcanism on the Hikurangi Plateau.

An electrically heterogeneous forearc

In the forearc (Fig. 2), high conductivity within 1 km of the seafloor is consistent with shipboard logging while drilling measurements at IODP Site U1519[30]. Below the frontal wedge, a small conductive anomaly (C4f) near the décollement is correlated with high-amplitude reflectivity (Fig. 2c). This may indicate subduction of conductive volcaniclastics analogous to those imaged at the base of SU8 in the Hikurangi Trough or the sediments associated with conductor C3p, assuming this layer extends northwest of the volcanic cones imaged beneath the Hikurangi Trough. Interestingly, C4f and the associated reflectivity do not extend down-dip of the second active thrust.

Landward of the frontal wedge, forearc resistivity becomes highly heterogeneous as three main conductors (C1f, C2f, and C3f) appear embedded in a more resistive background. These conductors occur in locations devoid of clear stratigraphic layering in the seismic reflection data (Fig. 2c). However, in the case of C2f and C3f, the conductors correlate with higher-amplitude, albeit chaotic, reflectivity within the forearc wedge. Seismically imaged thrust faults[11,31] bound the landward side of C2f and the base of C3f while other thrust faults appear to coincide with narrow conductors that extend from C3f to ridges on the seafloor (Extended Data Fig. 1), suggesting that these faults separate zones of distinct porosity and may in some cases act as pathways for fluid release that manifest as seeps on the seafloor[32]. Interestingly, numerous seeps are found on the seafloor above C1f and C3f, whereas few appear above C2f (Fig. 2a & c). This may be due to the contrast in material properties around each conductor. While C1f and C3f are both overlain by conductive material, C2f is surrounded by a resistive, low-porosity halo that may inhibit fluid drainage to the seafloor (Fig. 2a & b).

At depth, the subducting slab is apparent as a sudden, rapid increase in resistivity (≥ 25 Ω-m) that dips below the seismically determined décollement (Fig. 2a & c). The smooth surface of the slab is interrupted by a cone-like feature (R1f) 33 km landward of the trench that juts 3 km above its surroundings. R1f occurs within the seismically defined envelope of a subducting seamount[11,31], however the resistor is peaked and occupies the downdip half of the seamount geometry inferred from seismic reflection and magnetic anomaly observations[8]. High wavespeeds (Vp >5 km/sec) from a high-resolution 3D tomographic inversion are well correlated with the dimensions of R1f, and were interpreted as indicating that the seamount is either 1) smaller and located further down-dip than previously thought or 2) characterised by low velocities[33]. Our observations from Tūranganui Knoll present a third alternative, which is that the internal structure of the subducting seamount may be similarly heterogeneous. Specifically, we interpret R1f to be the core of a subducting seamount, comparable in structure to R1p of Tūranganui Knoll. This resistive core (R1f) is blanketed by a swath of more conductive material analogous to C1p of Tūranganui Knoll. The presence of a broad, resistive cap similar to R2p at Tūranganui Knoll is consistent with magnetic anomaly observations[8]. However our synthetic inversion of a subducted seamount whose electric structure is equivalent to that of Tūranganui Knoll shows that our data cannot resolve such a thin feature at depth (Extended Data Fig. 3).

From our porosity estimates we find that, in addition to being conspicuously conductive, C1f, C2f, and C3f also correspond to fluid-rich anomalies (Fig. 2b). The porosity of these conductors is generally greater than the neighboring forearc and may indicate zones of elevated pore fluid pressure. The locations of these conductors coincide with a region of widespread underconsolidation and elevated porosity that geodynamic models predict to be generated above and in the wake of subducting seamounts[34].

Seamount structure influences slow slip

Intriguingly, a number of burst-type repeating earthquakes and microseismicity associated with the September—October 2014 SSE offshore Gisborne, North Island, New Zealand[7] cluster in and around C2f in the upper plate (Fig. 2a & b). These burst-type repeaters have been linked to aseismic slip and fluid migration, and our model reveals their association with a region of anomalously high porosity directly above the subducting seamount. Our observation provides in-situ evidence that not only links subducting topography to the creation of interconnected fluidized networks in the forearc, but also demonstrates that such fracture networks can host microseismicity and fluid transfer through damage associated with the interaction between the downgoing seamount and overriding plate (Fig. 3).

Intraplate seamount formation involves a build-up of effusive flows that become overlain by higher porosity, volcaniclastics and vesicular basalts, imparting seamounts with both a strong core and highly porous component. Therefore, it is not unreasonable to assume that the resistivity structure of the subducting seamount is similar to Tūranganui Knoll. In particular, we suggest that the subducting seamount also contains a resistive core (R1f) embedded within an overlying matrix of porous, conductive material. The presence of a low permeability, basaltic cap (R2p) at the top of the subducting seamount is supported by magnetic anomaly data[8]. Upon subduction, we propose that this cap would have initiated fracturing in the upper plate that persisted through a structurally competent core. Observations of increased shear wave splitting delay times preceding the September—October 2014 SSE[35] suggest that fluid overpressure accumulated within the subducting plate[36] before slip. This stress change, along with dehydration reactions within the seamount that would further have contributed to elevated pore fluid pressure, may have induced hydrofracturing[37] and brittle deformation of the low permeability basaltic cap. Focal mechanisms reveal that extensional and strike-slip faulting within the subducting plate preceded the 2014 SSE[36], and we posit that some of these events may have been associated with fracturing of the cap. Once the cap ruptured, fluids in the underlying conductive porous matrix (C1p) could escape and vertically migrate across the subduction interface and into the topography-induced fracture networks of the overthrusting forearc. The transfer of fluids and overpressure from the subducting slab to the overriding plate is consistent with changes in the stress tensor and Vp/Vs ratios before and during the September—October 2014 SSE[35,36] (Fig. 3).

Because lithostatic pressure increases with depth, fractures in the subducting seamount and upper plate should not remain open indefinitely even though microporosity resulting from damage may persist (Fig. 3c). Rather such fracturing might occur episodically as the subducting topography experiences changes in the stress regime that lead to fluctuations in pore fluid pressure[36]. Episodic rupturing and closing of these fractures, especially in the basaltic cap, may promote cyclic fluid drainage[38] from the subducting seamount into the overriding plate. Retention of high conductivity in C2f suggests the persistence of weakened zones within the forearc and may indicate the inability of fluids to completely escape the damaged upper plate, which could be related to the resistive, low-porosity halo surrounding C2f and a conspicuous deficiency in surface seeps[32] (Fig. 2a & b). Cementation through hydrothermal activity is also a mechanism capable of sealing off pathways to the seafloor after fluid injection[39].

The natures of C1f and C3f are more enigmatic. Both may be related to damage incurred by the presently imaged subducting seamount or by the passage of previous seamounts now located farther downdip. The proximity of C1f to the seismic high reflectivity zone (HRZ), which is purported to be a package of water-rich sediments at the toe of the subducting seamount[31] and is correspondingly more conductive than R1f, may alternatively indicate a hydrologic connection between these features whereby water released from the HRZ preferentially flows into C1f. This connection may be locally enhanced by higher structural permeability associated with this section of the forearc being in an extensional stress regime in contrast to the region nearer the trench, which is in compression[33,35] (Fig. 2a). The location and conductivity of C3f are consistent with sediments underplated beneath the outer forearc in a manner similar to that observed in Nankai[40]. It has been speculated that low rigidity material within an accretionary wedge may contribute to tsunami generation during earthquakes[40], and we note that the 1947 Offshore Poverty Bay tsunami earthquake[41] occurred near C3f (Fig. 2a & b). Whether C3f is the result of sediment underplating or seamount damage, active deformation is required to explain its inferred high porosity.

Noticeably absent from our resistivity model (Fig. 2) is an elongated, conductive channel along the décollement associated with porous subducting sediments, which has been observed at other erosive margins[14,42]. While the resistivity and porosity of the HRZ[31] are consistent with compacting sediments, and there is evidence of subducting sediment near the trench (C4f; Fig. 2a—c), the top of the seamount appears to lack a high conductivity channel, which indicates that the plate interface is locally starved of water-rich sediments. This deficiency permits a more direct contact between the competent subducting seamount and upper plate, and contributes to geometric and lithologic heterogeneity in megathrust properties[11].

The absence of porous sediments at the plate interface in this area suggests that the primary source of fluids responsible for the observed variations in effective stress[36] and Vp/Vs[35] comes from water trapped within the subducting seamount in addition to water from subducted sediments downdip within the HRZ. The higher permeability of the subducting seamount relative to any surrounding sediments[26] might also support concentrated fluid flow through the seamount. Our results imply that the interaction of subducting seamounts with the overriding plate serves to create randomly oriented fracture planes that lead to a heterogeneous stress distribution in the seismogenic zone[4,43], and also to pore pressure transfer from the seamount to the forearc through episodic fluid release[38] (Fig. 3). We hypothesize that these dual effects of subducting topography are partly responsible for along-strike variations in interseismic coupling at the Hikurangi Margin[10,44] and may be occurring globally in regions that experience slow slip where subducting topography is present. Furthermore, our data demonstrate that seamounts can hold a previously unrecognized and substantial volume of water. Based on approximations of the global abundance of intraplate volcanism[45] and the porosity structure of Tūranganui Knoll, we estimate that subducting topography contributes at least 5.5—9.4 x 10^6 Tg/Myr of water to the deep Earth, providing localized fluid enhancement from particularly rough slabs.

References

1. Cloos, M. Thrust-type subduction-zone earthquakes and seamount asperities: a physical model for seismic rupture. *Geology* **20**, 601–604 (1992).
2. Scholz, C. H. & Small, C. The effect of seamount subduction on seismic coupling. *Geology* **25**, 487–490 (1997).
3. Singh, S. C. *et al.* Aseismic zone and earthquake segmentation associated with a deep subducted seamount in Sumatra. *Nat. Geosci.* **4**, 308–311 (2011).
4. Wang, K. & Bilek, S. L. Do subducting seamounts generate or stop large earthquakes? *Geology* **39**, 819–822 (2011).
5. Bassett, D. & Watts, A. B. Gravity anomalies, crustal structure, and seismicity at subduction zones: 1. Seafloor roughness and subducting relief. *Geochemistry, Geophys. Geosystems* **16**, 1508–1540 (2015).
6. Dominguez, S., Lallemand, S. E., Malavieille, J. & Von Huene, R. Upper plate deformation associated with seamount subduction. *Tectonophysics* **293**, 207–224 (1998).
7. Shaddox, H. R. & Schwartz, S. Y. Subducted seamount diverts shallow slow slip to the forearc of the northern Hikurangi subduction zone, New Zealand. *Geology* **47**, 415–418 (2019).
8. Barker, D. H. N. *et al.* Geophysical constraints on the relationship between seamount subduction, slow slip, and tremor at the North Hikurangi subduction zone, New Zealand. *Geophys. Res. Lett.* **45**, 804–813 (2018).
9. Davidson, S. R. *et al.* Conjugate strike-slip faulting across a subduction front driven by incipient seamount subduction. *Geology* **48**, 493–498 (2020).
10. Wallace, L. M. *et al.* Characterizing the seismogenic zone of a major plate boundary subduction thrust: Hikurangi Margin, New Zealand. *Geochemistry, Geophys. Geosystems* **10**, (2009).
11. Barnes, P. M. *et al.* Slow slip source characterized by lithological and geometric heterogeneity. *Sci. Adv.* **6**, 1–11 (2020).
12. Evans, R. L. Constraints on the large-scale porosity and permeability structure of young oceanic crust from velocity and resistivity data. *Geophys. J. Int.* **119**, 869–879 (1994).
13. Naif, S., Key, K., Constable, S. & Evans, R. L. Water-rich bending faults at the Middle America Trench. *Geochemistry*

Geophys. Geosystems **16**, 2582–2597 (2015).

14. Naif, S., Key, K., Constable, S. & Evans, R. L. Porosity and fluid budget of a water-rich megathrust revealed with electromagnetic data at the Middle America Trench. *Geochemistry Geophys. Geosystems* **17**, 2825–2834 (2016).
15. Johansen, S. E. *et al.* Deep electrical imaging of the ultraslow-spreading Mohns Ridge. *Nature* (2019).
16. Chesley, C., Key, K., Constable, S., Behrens, J. & Macgregor, L. Crustal cracks and frozen flow in oceanic lithosphere inferred from electrical anisotropy. *Geochemistry, Geophys. Geosystems* 1–21 (2019).
17. Barker, D. H. N., Sutherland, R., Henrys, S. & Bannister, S. Geometry of the Hikurangi subduction thrust and upper plate, North Island, New Zealand. *Geochemistry Geophys. Geosystems* (2009).
18. Wallace, L. M. *et al.* Hikurangi subduction margin coring, logging, and observatories. *Proc. Int. Ocean Discov. Progr. 372B/375 Coll. Station. TX (International Ocean Discov. Program).* 5–10 (2019).
19. Wallace, L. M. *et al.* Slow slip near the trench at the Hikurangi subduction zone, New Zealand. *Science (80-.).* **352**, 701–704 (2016).
20. Taylor, B. The single largest oceanic plateau : Ontong Java – Manihiki – Hikurangi. *Earth Planet. Sci. Lett.* **241**, 372–380 (2006).
21. Key, K. MARE2DEM: A 2-D inversion code for controlled-source electromagnetic and magnetotelluric data. *Geophys. J. Int.* **207**, 571–588 (2016).
22. Davy, B., Hoernle, K. & Werner, R. Hikurangi Plateau: Crustal structure, rifted formation, and Gondwana subduction history. *Geochemistry, Geophys. Geosystems* **9**, (2008).
23. Wallace, L. M. *et al.* Site U1526. *Wallace, L.M., Saffer, D.M., Barnes, P.M., Pech. I.A., Petronotis, K.E., LeVay, L.J., Exped. 372/375 Sci. Hikurangi Subduction Margin Coring, Logging, Obs. Proc. Int. Ocean Discov. Program, 372* **372**, (2019).
24. Pezard, P. A. Electrical properties of mid-ocean ridge basalt and implications for the structure of the upper oceanic crust in Hole 504B. *J. Geophys. Res.* **95**, 9237–9264 (1990).
25. Antriasian, A. *et al.* Thermal regime of the Northern Hikurangi Margin, New Zealand. *Geophys. J. Int.* 1177–1190 (2018).
26. Fisher, A. T. & Wheat, C. G. Seamounts as conduits for massive fluid, heat, and solute fluxes on ridge flanks. *Oceanography* **23**, 74–87 (2010).
27. Archie, G. E. The electrical resistivity log as an aid in determining some reservoir characteristics. *Trans. AIME* **146**, 54–62 (1942).

28. Becker, K. Large-scale electrical resistivity and bulk porosity of the upper oceanic crust at Hole 395A. *Proc., Sci. results, ODP, Legs 106/109, Mid-Atlantic Ridge* **106**, 205–212 (1990).

29. Barnes, P. M. *et al.* Site U1520. *Wallace, L.M., Saffer, D.M., Barnes, P.M., Pech. I.A., Petronotis, K.E., LeVay, L.J., Exped. 372/375 Sci. Hikurangi Subduction Margin Coring, Logging, Obs. Proc. Int. Ocean Discov. Program, 372* (2019).

30. Barnes, P. M. *et al.* Site U1519. *Wallace, L.M., Saffer, D.M., Barnes, P.M., Pech. I.A., Petronotis, K.E., LeVay, L.J., Exped. 372/375 Sci. Hikurangi Subduction Margin Coring, Logging, Obs. Proc. Int. Ocean Discov. Program, 372* (2019).

31. Bell, R. *et al.* Seismic reflection character of the Hikurangi subduction interface, New Zealand, in the region of repeated Gisborne slow slip events. *Geophys. J. Int.* **180**, 34–48 (2010).

32. Watson, S. J. *et al.* Focused fluid seepage related to variations in accretionary wedge structure, hikurangi margin, New Zealand. *Geology* **48**, 56–61 (2020).

33. Arai, R. *et al.* Three-dimensional P-wave velocity structure of the northern Hikurangi margin from the NZ3D experiment: Evidence for fault-bound anisotropy. *J. Geophys. Res. Solid Earth* (2020).

34. Sun, T., Saffer, D. & Ellis, S. Mechanical and hydrological effects of seamount subduction on megathrust stress and slip. *Nat. Geosci.* **13**, (2020).

35. Zal, H. J. *et al.* Temporal and spatial variations in seismic anisotropy and Vp/Vs ratios in a region of slow slip. *Earth Planet. Sci. Lett.* **532**, 115970 (2020).

36. Warren-Smith, E. *et al.* Episodic stress and fluid pressure cycling in subducting oceanic crust during slow slip. *Nat. Geosci.* **12**, 475–481 (2019).

37. Bonnet, G., Agard, P., Angiboust, S., Fournier, M. & Omrani, J. No large earthquakes in fully exposed subducted seamount. *Geology* **47**, 407–410 (2019).

38. Nakajima, J. & Uchida, N. Repeated drainage from megathrusts during episodic slow slip. *Nat. Geosci.* **11**, 351–356 (2018).

39. Sibson, R. H. Stress switching in subduction forearcs: Implications for overpressure containment and strength cycling on megathrusts. *Tectonophysics* **600**, 142–152 (2013).

40. Park, J. O. *et al.* A low-velocity zone with weak reflectivity along the Nankai subduction zone. *Geology* **38**, 283–286 (2010).

41. Bell, R., Holden, C., Power, W., Wang, X. & Downes, G. Hikurangi margin tsunami earthquake generated by slow

seismic rupture over a subducted seamount. *Earth Planet. Sci. Lett.* **397**, 1–9 (2014).
42. Li, J. *et al.* Connections between subducted sediment, pore-fluid pressure, and earthquake behavior along the Alaska megathrust. *Geology* **46**, 299–302 (2018).
43. van Rijsingen, E., Funiciello, F., Corbi, F. & Lallemand, S. Rough subducting seafloor reduces interseismic coupling and mega-earthquake occurrence : Insights from analogue models. *Geophys. Res. Lett.* 3124–3132 (2019).
44. Wallace, L. M. Slow Slip Events in New Zealand. *Annu. Rev. Earth Planet. Sci.* **48**, 175–203 (2020).
45. Conrad, C. P., Selway, K., Hirschmann, M. M., Ballmer, M. D. & Wessel, P. Constraints on volumes and patterns of asthenospheric melt from the space-time distribution of seamounts. *Geophys. Res. Lett.* **44**, 7203–7210 (2017).

Main Figure Legends

Figure 1. Tectonic setting and HT-RESIST survey area. a) Regional tectonic map of Hikurangi Margin. White arrows indicate convergence rate and direction of the Pacific Plate relative to the Australian Plate in mm/yr. Shaded contours are cumulative slip patches in 100 mm (red and blue) or 20 mm (green) contour intervals: Red - SSEs from 2002-2014; Green - deep slip associated with 2006 and 2008 SSE; Blue - afterslip from 2016 Kaikoura earthquake (see ref. [44] and refs therein). Taupo VZ = Taupo Volcanic Zone. b) Close up map of survey region (purple square shown in panel a). High resolution bathymetry data in b) were provided courtesy of the National Institute of Water and Atmospheric Research (https://niwa.co.nz/). Gray squares show EM receivers used in this survey. Red circles are the locations of IODP drilling sites[18] in the region. Red contours are slip from the September-October 2014 SSE. Each contour is 50 mm of slip[19]. White line is the 6.75 km depth contour of the subducting seamount inferred from magnetic data[8]. Cyan squares are areas with evidence of fluid seeps[32]. White stars are repeating earthquakes associated with the 2014 SSE[7], and blue star shows the epicenter of the 1947 Offshore Poverty Bay tsunami earthquake[41].

Figure 2. Preferred resistivity model and porosity with key features labeled and seismic interpretations overlain. a) Vertical resistivity model, b) porosity estimated using Archie's Law[27], and c) & d) available co-located seismic reflection data from profile 05CM-04[8] overlain on resistivity. See text for discussion of prominent conductors (C1p, C2p, C3p, C1f, C2f, C3f, and C4f) and resistors (R1p, R2p, R2.5p, and R1f). Black inverted triangles are receivers where MT and CSEM data were used in the inversion; green circles are receivers where only CSEM data were inverted. Available along-profile heat flow data on the incoming plate from ref. [25] are plotted as red circles in a) & b). 58±8 mW/m^2 is the average background heat flow, denoted by the dashed red line. HRZ is the seismic high reflectivity zone discussed in ref. [31]. Relocated burst-type repeating earthquakes (white stars) and general seismicity (white circles) associated with the September-October 2014 slow slip event

within 10 km of the profile[7] are shown in a) & b). The average error in the horizontal and vertical locations of the relocated events is 790 m and 720 m, respectively[7]. Blue star is the projected location of the 1947 Offshore Poverty Bay tsunami earthquake[11,41] (same as Fig.1). Active fluid seeps within 10 km of the profile from ref. [32] are also shown as cyan squares. The 5 km/s Vp contour[33] near R1f is shown as a purple dashed line. The areas of extension and compression in the forearc from ref. [33] are denoted at the top of a). Seismically interpreted structures[11,17] and magnetic basement[8] are coded in the legend in b).

Figure 3. Schematic representation of fluid transfer from subducting topography to the overthrusting forearc during a slow slip cycle. The topography has a hypothetical structure that would exhibit a resistivity similar to Tūranganui Knoll—a resistive core of intrusives; a porous amalgam of volcaniclastics, pre-eruptive sediments, and hydrothermal minerals; a resistive cap of basalt; and a veneer of marine sediments. a) Subducting topography transports water to the subduction zone and damages the upper plate as it subducts. Pore fluid pressure builds in the slab and subducting topography and decreases in the upper plate[35,36]. b) Stress builds up in the subducting topography and causes it to deform. Dehydration reactions may release mineral-bound fluids and promote hydrofracturing. Just before the SSE, the relatively low permeability, resistive cap breaks and fluids escape into the upper plate damage zone, which decreases pore pressure in the topography while increasing it in the overriding plate[35,36]. c) After the SSE, much of the fluid will escape, decreasing pore pressure in the upper plate[35]. Structural barriers and cementation in the overriding plate do not permit complete fluid escape. Fractures in the subducting topography close and the cycle begins again as pressure builds in the subducting topography. d)—f) Schematic trends in pore fluid pressure evolution for the upper plate (orange) and subducting slab (blue) during a)—c). These trends are based on the work of ref. [36] and ref. [35], that examine stress ratio and Vp/Vs time series, respectively, for the September—October 2014 SSE. Locations where these changes would be observed are shown as similarly colored dots in a)—c).

1 METHODS

1.1 EM Data Collection

We collected CSEM and MT data on 29 ocean-bottom electromagnetic (OBEM) receivers during December 2018—January 2019 for the Hikurangi Trench Regional Electromagnetic Survey to Image the Subduction Thrust (HT-RESIST). The Mk III broadband OBEM receivers use 10 m long electric dipoles and induction coil magnetometers capable of measuring orthogonal, horizontal electric and magnetic field components in the 0.0001-500 Hz frequency band[46]. This broadband recording capacity allows for the simultaneous collection of high frequency CSEM and longer-period MT data. The OBEMs recorded with a 125 Hz sampling rate. OBEMs were deployed along a 90 km transect that crosses the Hikurangi deformation front (Fig. 1) and is co-located with seismic reflection line 05CM-04[17] and IODP Sites U1518, U1519, U1520, and U1526[18]. The ~3 km station spacing helps to ensure that features in the resistivity model are constrained by data from more than one receiver.

To collect CSEM data, we deep-towed the Scripps Undersea Electromagnetic Source Instrument (SUESI) close to the seabed at an altitude of approximately 100 m to minimize signal attenuation through seawater[46]. During the tow, SUESI output a 250—300 A alternating current across a 293 m horizontal electric dipole terminated by copper electrodes. We used the complex binary Waveform D of ref. [47] with a fundamental transmission period of 4 s while towing over 26 of the 29 OBEMs. Waveform D is a doubly symmetric waveform designed to spread the high power harmonics over about a decade of frequency, thus allowing for constraints on the resistivity structure at different length scales[47]. Due to a recording issue during the first deployment, three OBEMs (stations 16-18) were redeployed and recorded data from an additional tow using a source waveform with a 6 s fundamental period. We determined SUESI's position using an inverted long-baseline acoustic navigation system[48].

1.2 CSEM and MT Data Processing

Overall, the OBEMs recorded good quality data but we discarded data from two OBEMs (stations 4 and 25) due to poor electrode connections. CSEM amplitude and phase responses at the strongest harmonics of waveform D were computed using a robust stacking method to reduce bias and increase the signal-to-noise ratio[47]. The time series were divided into windows whose length is the fundamental period of the transmitted waveform (either 4 s or 6 s). These sections were then pre-whitened, Fourier transformed, and post-darkened to produce Fourier coefficients. The Fourier coefficients were normalized by the complex source dipole moment and corrected for the individual sensor responses of each OBEM. The Fourier coefficients were then stacked into 120 s segments using an algorithm that iteratively removes outliers. The variance of each stack, and hence the data error, was assigned based on the stack residuals.

Inline CSEM data are primarily sensitive to resistivity variations within the vertical plane between the source dipole and the OBEM, making 2-D modelling of these data appropriate (see ref. [21] and references therein). In our inversions, we used CSEM data at the three strongest harmonics of waveform D (1st, 3rd, and 7th) from all OBEMs. We also used higher frequencies (up to 8.25 Hz) where good quality, long-offset data were present, which was particularly the case for OBEMs located on the Tūranganui Knoll. We omitted all data at transmitter-receiver offsets $\leq$ 2 km as these data are most susceptible to error based on navigational uncertainty[49]. We also removed any obvious outliers that remained after stacking and we discarded data with signal-to-noise ratios $\geq$ 2. We applied a 2% error floor to data collected when the source was transmitting at the 4 s fundamental period and a slightly larger error floor of 3% to data from the three receivers that collected data at the 6 s fundamental period. This was done to avoid overfitting data variations due to small bathymetric differences between the two towpaths. Example CSEM responses at 0.75 Hz for a station on the forearc and another station on the incoming plate are shown in Extended Data Fig. 4.

To estimate impedance tensors from the MT data, we used the robust multiple-station approach of ref. [50]. This yielded high quality MT responses at about 20—3000 s period, with the short period limit reaching 11 s for the shallowest OBEMs and 26 s for the deep-water OBEMs. Impedance polar diagrams (Extended Data Fig. 5) show 1-D to 2-D compatible MT responses at shorter periods for the forearc stations whereas the longer period data and incoming plate stations have polar diagrams exhibiting 3-D induction effects, which cannot be accurately modelled using MARE2DEM[21]. Therefore, we limited the inverted MT data to only the shorter period, 1-D and 2-D compatible data from 14 forearc stations. We determined the strike direction (Extended Data Fig. 5) by fitting a line to the transmitter and OBEM positions so that the strike is the average profile direction. We note that this definition of the strike is necessary when modeling inline CSEM data and is also reasonable for the MT data we inverted given their impedance polar diagrams. We assigned a 10% error floor to the inverted MT data.

1.3 CSEM and MT Joint Inversion

We performed joint, nonlinear, regularized inversion of the CSEM and MT data using MARE2DEM[21]. We inverted the CSEM data as $\log_{10}$ amplitude and phase and the MT data as $\log_{10}$ apparent resistivity and phase because these data scalings have been shown to lead to more robust and efficient convergence to a low RMS[51]. Initial isotropic inversion revealed characteristic anisotropy artefacts, so we inverted for transverse vertical isotropy in which the horizontal components of resistivity comprise the plane of isotropy and the resistivity tensor has the form:

$$\rho = \begin{pmatrix} \rho_h & & \\ & \rho_h & \\ & & \rho_v \end{pmatrix} \tag{1}$$

where ρ_h and ρ_v are the horizontal and vertical resistivity, respectively. The inversion scheme solved for these components in 56,666 cells. To avoid biasing our inversion by structure in the input starting model, we used a 1 Ω-m uniform halfspace as the starting model for the inversion. Our preferred model converged with an RMS misfit of 0.998 and has only a small amount of anisotropy (average absolute ratio is 1.2x from the seafloor to a depth of 6.5 km; Extended Data Fig. 6b). The misfit breakdown is shown in Extended Data Fig. 7. Because there are more CSEM data than MT, and because CSEM data are most sensitive to the vertical resistivity component, we show the vertical resistivity in Fig. 2 and Extended Data Fig. 1 and the horizontal resistivity and anisotropy ratio in Extended Data Fig. 6. Model fits for the CSEM data at the three highest power harmonics are shown in Extended Data Fig. 8. MT data and model responses are shown in Extended Data Fig. 9. Most of the data are fit to RMS 1.0 or better (Extended Data Fig. 7). The largest misfit is for CSEM data around the trench axis (0 km position) where a small fraction of the normalized residuals reach as high as RMS 2.5. This is most likely a result of slight inconsistencies between the two tows as data from the second tow spans from -9 km to 4 km.

1.4 Sensitivity to Forearc Conductors and Subducting Topography

To determine whether or not forearc conductors C1f, C2f, and C3f are required by our data, we forward modeled the response of our preferred model with each conductor reassigned to a more resistive value. These conductors have resistivity around 1—3 Ω-m and in our sensitivity tests we increased them to 5 and 10 Ω-m. These tests increased the overall RMS misfit from 0.998 to 0.999 (C1, 5 Ω-m), 1.001 (C1, 10 Ω-m), 1.011 (C2, 5 Ω-m), 1.038 (C2, 10 Ω-m), 1.212 (C3, 5 Ω-m), and 1.958 (C3, 10 Ω-m). Extended Data Fig. 10 shows more detailed local RMS changes as a function of CSEM transmitter position and MT receiver location. These tests confirm that our data are sensitive to C1f, C2f, and C3f as perturbing these features significantly increased the local data misfits. As expected, the data are more sensitive to C2f and C3f because they are shallower and more conductive than C1f. Nevertheless, these tests demonstrate that each forearc conductor is required to fit the data.

We also tested the sensitivity to resistor R1f by decreasing its resistivity to 20, 10 and 7 Ω-m, which increased the data misfit; Extended Data Fig. 11 shows that the MT data fits for stations above this feature become significantly worse as its resistivity is decreased. Thus R1f is required to fit the data. The CSEM data are insensitive to structure at this depth, and therefore the change in misfit was negligible.

1.5 Forearc Resolution Test

To assess the ability of these data to resolve features in a subducting seamount, we constructed a synthetic model with the approximate resistivity of the preferred model and a subducting Tūranganui Knoll in place of R1f. Using the same data density from our preferred model inversion, we generated synthetic data by adding 2% Gaussian noise to the forward response of Extended Data Fig. 3a. Inversion of these synthetic data (Extended Data Fig. 3b) from a 1 Ω-m uniform halfspace starting model converged to an RMS misfit of 1.004 with a 2% error floor. While the overall shape of the subducting seamount is resolved by the data, finer-scale features, such as the resistive cap (R2p), are smoothed through. This synthetic inversion also demonstrates the recoverability of more detailed structures in the Tūranganui Knoll on the incoming plate.

1.6 Porosity Estimation

We used the empirical Archie's Law[27] to convert our preferred resistivity model into porosity:

$$\phi = \left(\frac{\rho_f}{\rho} \right)^{\frac{1}{m}} \tag{2}$$

where ϕ is porosity, ρ is the bulk resistivity for which we have inverted, ρ_f is the pore fluid resistivity, and *m* is the cementation exponent. We assume the pore fluid has seawater salinity and computed its temperature-dependent resistivity using[52]

$$\rho_f^{-1} = 2.903916\left(1+0.0297175\mathrm{T}+1.5551\times10^{-4}\mathrm{T}^2\text{-}6.7\times10^{-7}\mathrm{T}^3\right) \tag{3}$$

For the temperature in each model cell, we used a linear geothermal profile:

$$T = T_0 + H\Delta z \tag{4}$$

where T_0 is temperature at the seafloor, which we extrapolated from temperature recorded by SUESI, *H* is the geothermal gradient based on records from IODP Sites U1518[53] (35˚C/km; forearc) and U1520[29] (38˚C/km; incoming plate), and Δz is depth below seafloor.

In Fig. 2b, we use *m*=2.4 based on resistivity studies in the southern Hikurangi Margin[54]. A smaller value for the cementation exponent has been used when considering fractured oceanic crust[13,28], so we include porosity calculated with *m*=2 in Extended Data Fig. 2b. Additionally, to show how varying the cementation exponent will affect the absolute porosity estimated from Archie's law, we offer several porosity conversions using a range of cementation exponents in Extended Data Fig. 2. We note that Archie's law might underestimate the porosity of intensely fractured rock and it will overestimate porosity where conductive mineral phases are present. Nevertheless, it provides a reasonable approximation of the relative porosity between features in the model.

1.7 Water Flux from Subducting Topography

To estimate the total contribution of water from subducting topography, we first approximate the volume flux of seamount material that undergoes subduction by computing the product of the global thickness of intraplate volcanism (24.1 m)[45] with the total length of subduction zones (3.8485×10^7 m) from ref. [55] and the weighted average of subducting plate velocities (6.237×10^{-2} m/yr)[55]. We convert this to a mass flux of water using the density of seawater at 0˚C (1027 kg/m^3), and our average porosity estimates for the Tūranganui Knoll (9.2%—13.2%). We also compute a slightly larger flux by assuming the volume of smaller seamounts in ref. [45] is constant (10.9 m) as a function of age but that their surface expressions are concealed by sediment over time. This would imply that the global thickness of intraplate volcanism is 28.8 m. The resulting flux (5.5—9.4×10^6 Tg/Myr) is likely an underestimate because it assumes all conductivity variations are due to pore fluid rather than mineral-bound water. Additionally, this estimate does not take into account the contribution of deeper hydration[56] that generates resistive alteration products (i.e. magnetite-poor serpentinite).

Data Availability

All EM data that were inverted and analysed in this study are available at https://doi.org/10.5281/zenodo.4721384 and as Source Data provided with this paper. The seismic reflection data overlain on the resistivity models are available at https://doi.org/10.21420/62C1-GS40.

Code Availability

A version of the MARE2DEM code used to invert the data is available at: http://mare2dem.bitbucket.io

Additional References

46. Constable, S. Review paper: Instrumentation for marine magnetotelluric and controlled source electromagnetic sounding. *Geophys. Prospect.* **61**, 505–532 (2013).

47. Myer, D., Constable, S. & Key, K. Broad-band waveforms and robust processing for marine CSEM surveys. *Geophys. J. Int.* **184**, 689–698 (2011).

48. Key, K. & Constable, S. Inverted long-baseline acoustic navigation of deep-towed CSEM transmitters and receivers. *Mar. Geophys. Res.* **42**, (2021).

49. Myer, D., Constable, S., Key, K., Glinsky, M. E. & Liu, G. Marine CSEM of the Scarborough gas field, Part 1: Experimental design and data uncertainty. *Geophysics* **77**, (2012).

50. Egbert, G. D. Robust multiple-station magnetotelluric data processing. *Geophys. J. Int.* **130**, 475–496 (1997).

51. Wheelock, B., Constable, S. & Key, K. The advantages of logarithmically scaled data for electromagnetic inversion. *Geophys. J. Int.* **201**, 1765–1780 (2015).

52. Constable, S., Key, K. & Lewis, L. Mapping offshore sedimentary structure using electromagnetic methods and terrain effects in marine magnetotelluric data. *Geophys. J. Int.* **176**, 431–442 (2009).

53. Saffer, D. M. *et al.* Site U1518. *Wallace, L.M., Saffer, D.M., Barnes, P.M., Pech. I.A., Petronotis, K.E., LeVay, L.J., Exped. 372/375 Sci. Hikurangi Subduction Margin Coring, Logging, Obs. Proc. Int. Ocean Discov. Program, 372*, (2019).

54. Schwalenberg, K., Rippe, D., Koch, S. & Scholl, C. Marine-controlled source electromagnetic study of methane seeps and gas hydrates at Opouawe Bank, Hikurangi Margin, New Zealand. *J. Geophys. Res. Solid Earth* **122**, 3334–3350 (2017).

55. van Keken, P. E., Hacker, B. R., Syracuse, E. M. & Abers, G. A. Subduction factory: 4. Depth-dependent flux of H_2O

from subducting slabs worldwide. *J. Geophys. Res. Solid Earth* **116**, (2011).

56. Park, J. & Rye, D. M. Broader impacts of the metasomatic underplating hypothesis. *Geochemistry, Geophys. Geosystems* **20**, 4810–4829 (2019).

Acknowledgements

We acknowledge that this work was partially carried out on the lands of the Te Āti Awa. We thank Scripps Institution of Oceanography for providing the instrumentation necessary to collect the EM data used in this study, the New Zealand government for permission to work in their exclusive economic zone, and the captains (W. Hill and D. Murline) and crew of the R/V Revelle Expeditions RR1817 and RR1903. Many thanks to S. Constable and the Scripps Marine EM Lab (C. Armerding, J. Lemire, J. Perez, J. Souders) and the HT-RESIST science party (A. Adams, J. Alvarez-Aramberri, C. Armerding, E. Attias, E.A. Bertrand, D. Blatter, G. Boren, G. Franz, C. Gustafson, W. Heise, Y. Li, B. Oryan, N. Palmer, J. Perez, J. Sherman, K. Woods, and A. Yates). We thank C. Rychert and M. Unsworth for their thorough and constructive comments as reviewers. We thank the National Institute of Water and Atmospheric Research (NIWA; https://niwa.co.nz/) for providing high-resolution bathymetry data. NIWA makes no representations or warranties regarding the accuracy or completeness of the data, the use to which data may be put, or the results that may be obtained from using the data, and NIWA accepts no liability for any loss or damage incurred by any person through the use of or reliance on the data. We acknowledge computing resources from Columbia University's Shared Research Computing Facility project, which is supported by NIH Research Facility Improvement Grant 1G20RR030893-01, and associated funds from the New York State Empire State Development, Division of Science Technology and Innovation (NYSTAR) Contract C090171, both awarded April 15, 2010. This work was supported by the National Science Foundation grant OCE-1737328. C.C. acknowledges funding support by the Department of Defense (DoD) through the National Defense Science and Engineering Graduate Fellowship (NDSEG) Program.

Author Contributions

S.N. and K.K. designed the experiment. S.N. and C.C. collected the data. C.C. and S.N. processed the data. C.C. modelled the data. All authors contributed to writing the manuscript.

Competing Interests Declaration

The authors declare no competing interests.

Extended Data Figure Legends

Extended Data Figure 1. Preferred inversion model (vertical resistivity component ρ_v) with high-resolution bathymetry. Seafloor receivers used in the inversion are gray cubes with station numbers. See Extended Data Fig. 6 for the horizontal resistivity and anisotropy. a) Northeast and b) southwest facing views of the bathymetry. High-resolution bathymetry were provided courtesy of the National Institute of Water and Atmospheric Research (https://niwa.co.nz/).

Extended Data Figure 2. Porosity conversion of the preferred resistivity model using a range of Archie's law cementation exponents. a) $m = 1.6$; b) $m = 2$; c) $m = 2.4$ (same as Fig. 2b); d) $m = 2.8$

Extended Data Figure 3. Resolution test of key model features. a) Model used to generate synthetic data. b) Model recovered from inversion of the synthetic data.

Extended Data Figure 4. Example of CSEM data and model responses from this survey. Amplitude and phase data (circles) and preferred model response (line) at 0.75 Hz for stations 7 (green) and 26 (blue) are shown. The rapid attenuation seen at station 7 and the much slower decay at station 26 are due to their respective locations on the conductive forearc and resistive Tūranganui Knoll.

Extended Data Figure 5. MT impedance polar diagrams shown as a function of period and station ID. Red and blue lines show $|Z_{xx}|$ and $|Z_{xy}|$, respectively, as a function of geographic rotation, with North pointing up. The black arrow in the white circle is the strike direction for this survey. Gray shading masks the periods and stations where data are omitted from our 2D analysis due to 3D effects in the polar diagram shapes.

Extended Data Figure 6. Vertical anisotropy of the preferred resistivity model. a) Horizontal resistivity (ρ_h) and b) anisotropy ratio (ρ_v / ρ_h). The model has minimal anisotropy.

Extended Data Figure 7. Preferred model root mean square (RMS) misfit breakdown. Normalized RMS for a) CSEM and b) MT data. Blue and red dots in a) are normalized residuals for all inline electric field amplitude and phase, respectively, at a given transmitter position. Bars in b) are RMS misfit for impedance tensor components of each MT receiver: blue-TE apparent resistivity; green-TE phase; orange-TM apparent resistivity; purple-TM phase.

Extended Data Figure 8. CSEM data (top), model fits (middle), and residuals (bottom) for the highest power harmonics as a function of distance from the Hikurangi Margin and transmitter-receiver offset. Dashed box indicates data collected at 1/6 Hz. All other data were collected at 1/4 Hz. a) Fundamental frequency, b) 3rd harmonic, and c) 7th harmonic.

Extended Data Figure 9. MT data and model responses. Fit of the preferred resistivity model (lines) to all MT data (circles) used in this study. TE mode is blue and TM mode is red.

Extended Data Figure 10. Sensitivity to forearc conductors C1f, C2f, and C3f. Change in model fit between the preferred model and forward models testing the sensitivity to the forearc conductors for the a) CSEM and b) MT data. To generate the top row of each panel, the resistivity of each conductor was individually increased to 5 Ω-m. The resistivity was increased to 10 Ω-m in the bottom panel. Blue and red dots in a) are the change in RMS for all inline electric field amplitudes and phases, respectively, at a given transmitter position. In b) bars are change in RMS misfit for impedance tensor components of each MT receiver: blue-TE apparent resistivity; green-TE phase; orange-TM apparent resistivity; purple-TM phase.

Extended Data Figure 11. Sensitivity to subducting seamount, R1f. Change in model fit between the preferred model and forward models testing the sensitivity to the subducting seamount for the MT data (CSEM data are insensitive to R1f). To generate the top, middle, and bottom panels, the resistivity of the subducting seamount was decreased to 20 Ω-m, 10 Ω-m, and 7 Ω-m, respectively. Bars are change in RMS misfit for impedance tensor components of each MT receiver: blue-TE apparent resistivity; green-TE phase; orange-TM apparent resistivity; purple-TM phase.

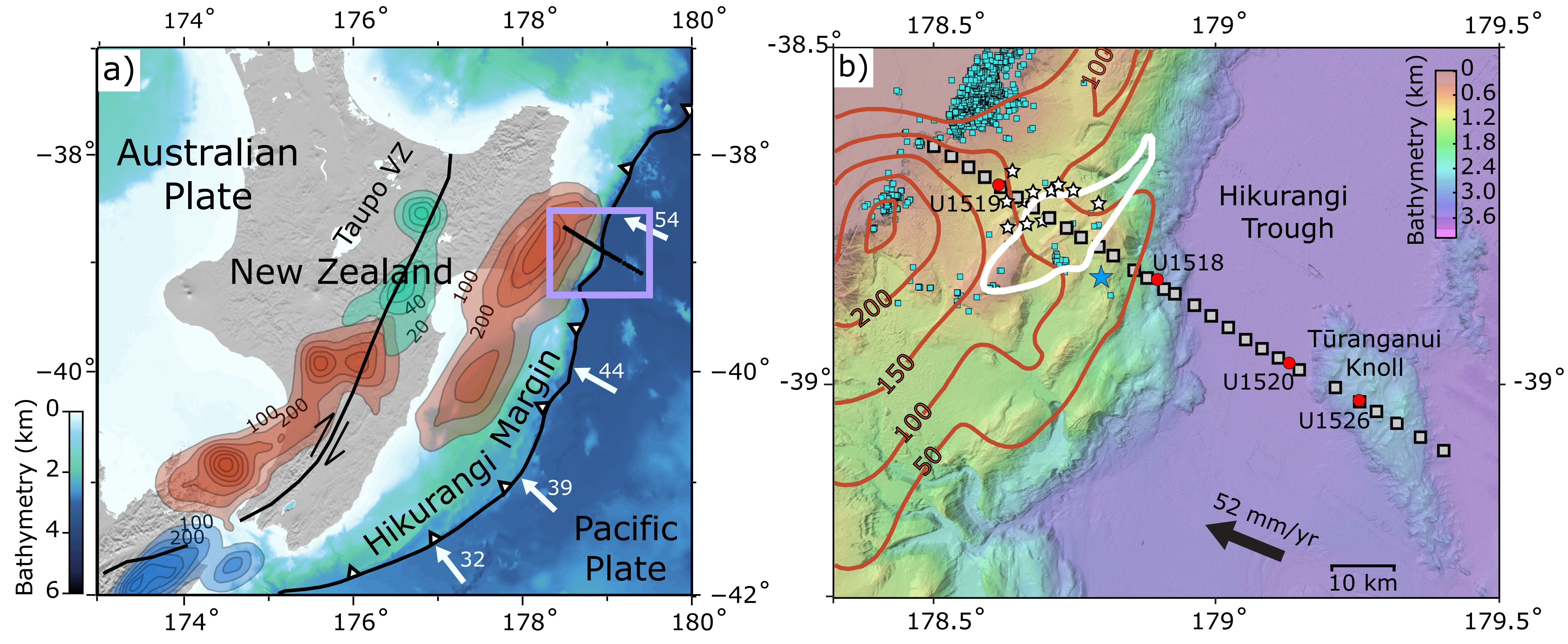
a)
Australian Plate
Taupo VZ
New Zealand
Hikurangi Margin
Pacific Plate
54
44
39
32
100
200
40
20
Bathymetry (km)
0
2
4
6
174°
176°
178°
180°
−38°
−40°
−42°
b)
Hikurangi Trough
Tūranganui Knoll
U1519
U1518
U1520
U1526
200
150
100
50
52 mm/yr
10 km
Bathymetry (km)
0
0.6
1.2
1.8
2.4
3.0
3.6
178.5°
179°
179.5°
-38.5°
-39°

a)
Extensional regime
Compressional regime
Heat flow (mW/m²)
Resistivity (Ωm)
Depth (km)
Distance from Hikurangi Deformation Front (km)
C1f
C2f
C3f
C4f
R1f
HRZ
R2p
R2.5p
C3p
C2p
C1p
R1p
Hikurangi Plateau
b)
Porosity
Normal fault
Décollement
Thrust fault
Thrust fault (inactive)
Base of Seismic Unit 8
Seismic reflection seamount
Magnetic basement - Barker et al. (2018)
5 km/s Vp contour - Arai et al. (2020)
Fluid seep - Watson et al. (2020)
1947 Offshore Poverty Bay Tsunami EQ - Bell et al. (2014)
Repeating EQ, relocated
General seismicity, relocated
Shaddox & Schwartz (2019)
Heat Flow - Antriasian et al. (2018)
c)
Tuaheni Basin
U1519
U1518
d)
Hikurangi Trough
Tūranganui Knoll
U1520
U1526

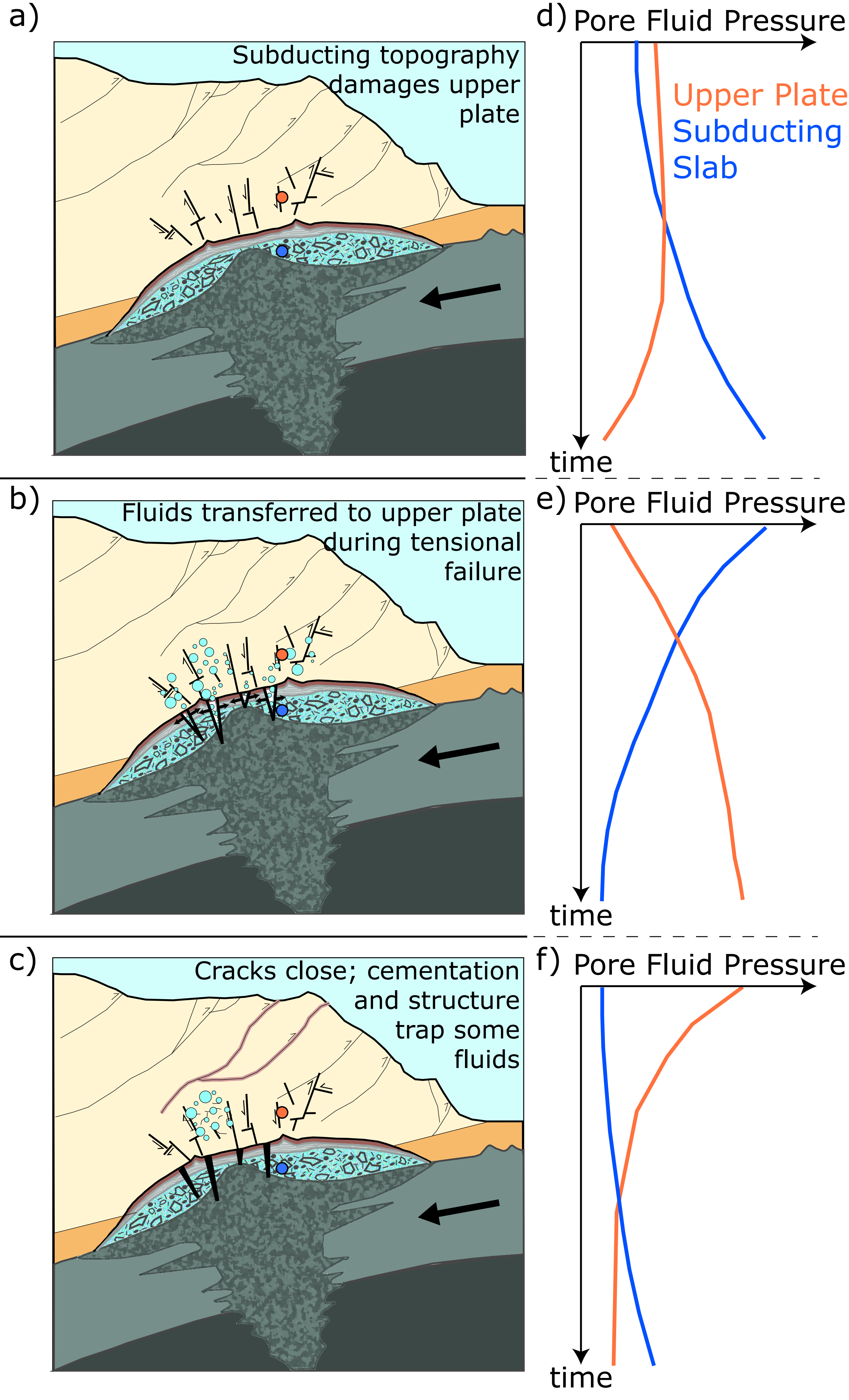
a)
Subducting topography damages upper plate
d) Pore Fluid Pressure
Upper Plate
Subducting Slab
time
b)
Fluids transferred to upper plate during tensional failure
e) Pore Fluid Pressure
time
c)
Cracks close; cementation and structure trap some fluids
f) Pore Fluid Pressure
time